



A Study into Surface-Piercing Propellers at Different Immersion Depths using a Towing Tank and a Numerical Method

M. Teimoori and M. S. Seif†

Marine Engineering Research Centre, Sharif University of Technology, Tehran, Iran

†Corresponding Author Email: seif@sharif.edu

(Received November 26, 2021; accepted June 5, 2022)

ABSTRACT

Surface-Piercing Propellers (SPPs) are essential categories of high-performance propulsion systems usually used for high-speed boats, which are designed to operate in semi-submerged conditions. In such conditions, a propeller performs in a two-phase mixed environment, consisting of water and air concurrently. Due to the intrinsic complexity of the working environment, describing the performance of an SPP is complex and cannot be recognized with the traditional submerged propellers. The present study aims to assess the effect of immersion depth on semi-submersible propellers. Accordingly, experimental tests in a towing tank were used along with a numerical method to achieve reliable results. In the numerical method, a sliding mesh was used to simulate the propeller's motion, and the volume of fluid was used to model the free surface. The hydrodynamic coefficients of the SPP, measured in the towing tank, were used to validate the numerical method. The outcomes of the numerical method were revealed to be in good agreement with the experimental data. The results showed that the critical advance coefficient decreased with the rise in the immersion depth. In detail, altering the immersion depth from 0.4 to 0.75 reduced the critical value of the advance coefficient from 0.8 to 0.7. The ventilation pattern also changed with increasing the immersion ratio. For a constant advance coefficient, the amount of ventilation increased at shallower depths of immersion.

Keywords: Semi submerged; Dynamometer; Simulation; Depth; Model test.

NOMENCLATURE

D	propeller's diameter	T	propeller's thrust
Fn	Froude number	u_i	speed in direction i
h	immersion depth of propeller	V_A	advance velocity
I_t	immersion ratio	Wn	Weber number
J	advance coefficient	Z	number of blades
K_Q	torque coefficient	γ	shaft yaw angle
K_T	thrust coefficient	η	efficiency
n	rotation rate of propeller	μ	viscosity
P	pressure	ρ	mass density
P/D	pitch ratio	σ	cavitation number
Q	propeller's torque	Ψ	shaft inclination angle
Rn	Reynolds number		

1. INTRODUCTION

Different propulsion systems, such as submerged propellers, surface-piercing propellers, and water jets, have been developed for high-speed crafts. The submerged propellers are the most common propellers used in the comprehensive type of ships. However, today, the use of semi-submersible

propellers has become widespread. One of the main differences between semi-submersible and conventional propellers is in their hydrodynamic performance. The diagram of thrust and torque coefficient against advance coefficient in a semi-submersible propeller can be divided into three parts, as shown in Fig. 1. The first phase is called the fully vented phase, the second phase is a transition, and the third phase is partially vented. The midpoint of

the transition zone denotes the critical advance coefficient. This point is the boundary between partial and complete ventilation.

Nowadays, given the high demand for surface-piercing propellers (SPPs) in a wide range of ships due to their excellent performance, numerous studies have been conducted on them. The studies performed so far can be divided into two categories: numerical and experimental ones.

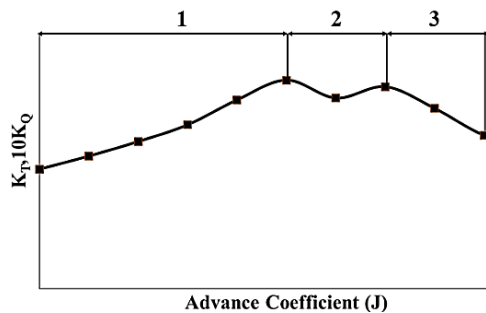


Fig. 1. K_T and K_Q coefficients of an SPP at different advance coefficients (Ghose 2004).

Most of the knowledge about the hydrodynamic parameters of SPPs has been obtained through experimental tests on models (Olofsson 1996). Shiba (1953) and Brandt (1973) analyzed the effect of critical Reynolds number, Froude number, and Weber number on the performance of an SPP. Hadler (1968), Kruppa (1972), Hecker (1973), Rains (1981), Rose and Kruppa (1991), Kruppa (1992), and Rose *et al.* (1993) were among those who conducted experimental research on the performance of SPPs between 1970 and 1990. They investigated the effects of various parameters such as the number of propeller blades, immersion ratio, pitch ratio, cross-section geometry, inclination, shaft yaw angle, rake, and skew angle on the hydrodynamic parameters of SPPs.

Olofsson (1996) experimentally investigated a partially submersible propeller's force and current properties. He found that at large Froude numbers in the partial ventilation zone, the effect of this number on the force coefficient is neglectable. Furthermore, by decreasing the Froude number, the force on the blades tends to increase. He also stated that the lower the Froude number, the less air is sucked into the depth, and therefore a greater force is needed due to the increased wet cross-section. Fernando *et al.* (2002) performed an experimental study on the hydrodynamic parameters of a series of SPPs with different blades, pitch ratios, immersion ratios, and shaft angles. They confirmed the results of Shiba (1953), which worked on the effect of Weber number on the critical advance coefficient. Misra *et al.* (2012) developed an SPP with four different cross-sections, pitch ratios, and expanded areas. They used propeller blades with wedge and diamond cross-sections. Three different wedge forms with angles of 0° , 30° , and 60° were constructed to study the effect of trailing edge angle (cup shape). According to the experimental results, for all ratios of immersion, the best performance was achieved by the 60-degree cup.

Numerical studies on SPPs can be divided into two categories: boundary element method and Reynolds Averaged Navier-Stokes (RANS) method. The boundary element method employs the lifting-line and vortex-lattice techniques to study the ventilation pattern of propellers, while the RANS method uses the finite volume method, as explained below. The first attempts for numerical modeling of semi-submersible propellers were made by Oberembt (1968) using the lifting line theory ignoring the wake changes and ventilation parameters. Wang and Jia (1990) used a lifting surface method to analyze a fully three-dimensional ventilation foil. They employed this method to evaluate the hydrodynamic performance of an SPP called MAU4-60. The obtained results were in good agreement with those of the simulation and experiments (Wang and Jia 1990; Wang *et al.* 1992). Savineau and Kinnas (1995) used the boundary element method to evaluate the performance of SPPs. Young and Kinnas (2003a,b 2004) used the three-dimensional boundary element method to predict the cavitation phenomenon in submerged propellers. They also used this method to study the behavior of supercavitation propellers and SPPs. They found that the amount of load on the key blade and aeration pattern agreed with the experimental results. Ghasemi *et al.* (2009) predicted the hydrodynamic parameters of two SPPs with three and six blades and different geometric characteristics using the boundary element method. They obtained the critical advance coefficient using the Weber number and the pitch ratio in the transient state and concluded that the efficiency of both propellers was greater than their completely submerged state. Yari and Ghassemi (2016a) developed a boundary element method to predict the performance and aeration pattern of an SPP. They validated the results with those of Olofsson (1996) and found a good agreement between the forces on a key blade obtained from numerical and experimental methods. In cases where the effects of viscosity and rotation should be considered, e.g., when investigating the three-dimensional changes of the free surface and separation due to the large angle of inclination and yaw angles of a shaft, it is necessary to use the RANS method (Young and Savander 2011).

Caponnetto (2003) was a pioneer in the analysis of semi-submersible propellers using the RANS method. He employed this method for a four-blade SPP. The results were in good agreement with the available data of the boundary element method and experimental tests. Kozłowska *et al.* (2011) used the RANS method to investigate the forces acting on a near-surface propeller during aeration. The obtained aeration regime agreed with the experimental results. However, in the ventilation mode, the forces were overestimated compared to the experimental results. Finally, Himei (2013) and Himei and Yamaguchi (2015) investigated semi-submersible propellers using the RANS method based on the VOF model. According to the results, at low advance coefficients, the torque coefficients were very different from the experimental values, while the thrust coefficient had a small error compared to the experimental results.

Applying the Unsteady RANS (URANS) method, Alimirzazadeh *et al.* (2016) investigated the performance of an SPP at different immersion ratios and yaw angles. They used the VOF model to simulate the free surface and the sliding mesh in their numerical work. They found that higher immersion ratios resulted in lower efficiency and higher thrust and torque coefficients. It was also found that the immersion ratio had a non-linear effect on the thrust and torque. In addition, the horizontal force and bending moment decreased when the immersion ratio grew up over 50% since the upper half of the propeller entered the water and generated a force. Yari and Ghassemi (2016b) used the RANS method to study the aeration, pressure distribution, and forces imposed on an SPP. They made a comparison to examine whether the numerical results matched the experimental ones, especially for high advance coefficients. They found that the cup significantly affected the ventilation pattern, pressure, and forces. The results indicated that the SPP thrust without a cup was lower than that of a propeller with a cup. Therefore, the efficiency was lower, as well. Yang *et al.* (2018) investigated the effect of artificial aeration on a semi-submersible propeller in fully submerged conditions using the URANS method. They stated that at high advance coefficients, artificial aeration increased the efficiency, while at low advance coefficients, the hydrodynamic performance of the propeller decreased. To increase the reliability of the predicted results from the numerical solution on the SPP, Nouroozi and Zeraatgar (2019) examined a semi-submerged propeller using a numerical solution and sliding mesh. They reported that conventional methods are not sufficient to determine the independence of mesh study. Therefore, they suggested that the mesh generation based on the ventilation pattern and turbulence parameters in the area near the tip, the leading and trailing edges on the suction side, and the recommended mesh base size in the stated section is 0.001diameter. Moreover, the best time step was correspondent with the rotation angle increment of 0.5°.

Javanmard *et al.* (2019) employed the URANS method to investigate the performance of semi-submersible propellers at different angular positions. They showed that at a specific advance coefficient, the thrust increased by changing the angular positions from 90° to 180°, and the maximum local thrust was near the leading edge. Meanwhile, from angular positions of 180° to 270°, the total thrust of the blade decreased, and the position of the maximum local thrust was away from the leading edge. Rad *et al.* (2019) investigated aeration patterns and the performance of semi-submersible propellers with five blades at different immersion depths using numerical simulations and laboratory investigations. According to the results, lower immersion ratios resulted in higher critical advance coefficient. Furthermore, with the rise in the advance coefficient, the length of the ventilation zone decreased, and consequently, the propeller was placed in a partially vented condition. Javanmard *et al.* (2020) studied the effect of shaft inclination angle on the hydrodynamic coefficients of SPPs and the fluid flow behavior around their key blades. They concluded that the

thrust and torque coefficients increased with the inclination angle. They also stated that with the raise in the shaft inclination angle, the maximum thrust and torque coefficient on the key blade occurred at lower rotation angles.

Since semi-submersible propellers are designed and manufactured to perform in both air and water, setting the optimal immersion depth is always a challenging problem in this field. In general, it seems that 50% of a propeller's diameter should be in the water, but regarding the diameter of the propeller hub, this value reaches about 40%. Nevertheless, the propeller may also work in other conditions, such as submerging the hub completely, for which 70% and 100% submerging are considered. Nevertheless, in practical operating conditions, the propeller starts from full submerging mode at low speeds and finally continues to move with low submerging at high speeds. Fig. 2 depicts a schematic of different immersion depths.

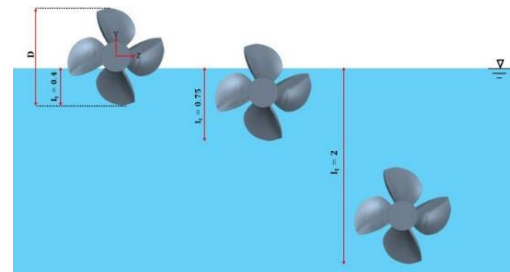


Fig. 2. A schematic of the propeller at different immersion ratios.

The propeller open-water test is usually performed in a cavitation tunnel. In this study, a towing tank was used to investigate the effects of immersion ratio so that the propeller could be tested in a completely submerged immersion condition. All of the effective parameters relative to the immersion ratio were also explored using a numerical solution in the STAR-CCM+ commercial software. The analysis was performed in an implicit unsteady open-water test using the sliding mesh method under free surface conditions. The thrust and moment coefficients of the SPP were calculated and compared with the experimental data. Furthermore, the six components of force and moment of the key blade and the ventilation pattern and pressure distribution on the propeller and key blade were investigated.

2. HYDRODYNAMIC CHARACTERISTICS OF THE PROPELLER

The dimensionless thrust and torque coefficients are widely used as well as efficiency for SPP performance evaluation (Eqs. 1-3, respectively).

$$K_T = \frac{T}{\rho n^2 D^4} \quad (1)$$

$$K_Q = \frac{Q}{\rho n^2 D^4} \quad (2)$$

$$\eta = \frac{K_T}{K_Q} \times \frac{J}{2\pi} \quad (3)$$

In the equations above, T and Q are the propeller's thrust and torque, respectively; n specifies the rotation rate; D indicates the propeller's diameter; ρ presents the mass density of water and J is the advance coefficient defined as Eq. (4).

$$J = \frac{V_A}{nD} \quad (4)$$

For an SPP, the operating conditions are as crucial as geometric parameters and affect its hydrodynamic parameters. Accordingly, the thrust and torque of a semi-submerged propeller are a function of the geometry and physical parameters, which include the advance coefficient (J), the Froude number (Fn), the Reynolds number (Rn), the cavitation number (σ), the Weber number (Wn), shaft inclination angle (ψ), shaft yaw angle (γ), pitch ratio (P/D), number of blades (Z), and the immersion ratio (I_t). Therefore, it can be said that the parameters affecting the performance of a semi-submersible propeller are as follows:

$$K_T \text{ \& } K_Q = F(J, F_n, R_n, \sigma, W_n, P/D, Z, I_t) \quad (5)$$

The Froude number, Weber number, Reynolds number, and immersion ratio, as the most important dimensionless numbers in SPP investigations, are presented in Eqs. (6) to (9) respectively:

$$F_n = \frac{nD}{\sqrt{gD}} \quad (6)$$

$$W_n = \frac{nD}{\sqrt{\frac{\sigma}{\rho D}}} \quad (7)$$

$$R_n = \frac{nD^2}{\nu} \quad (8)$$

$$I_t = \frac{h}{D} \quad (9)$$

where σ is the water's capillarity constant, exhibiting the kinematic viscosity of the water coefficient, and h denotes the immersion depth of the propeller. Brandt (1973) discovered that the effect of the Reynolds number is negligible if this number is greater than 5×10^5 . Therefore, in this study, these conditions were considered for Reynolds numbers to ignore its effects. In addition, inclination angle, yaw angle of shaft, number of blades, and pitch ratio were assumed to be constant to examine the effects of immersion ratio and advance velocity.

3. PROPELLER GEOMETRY AND EXPERIMENTAL TESTING

3.1 Propeller Geometry

The propeller's main characteristics and geometric parameters are given in Table 1. The propeller

considered for the experimental test was manufactured according to the ITTC (2005) instructions.

Table 1 Geometric characteristics of the propeller

Property	Magnitude
Model Propeller ID	CP002
Scale Ratio	1.0
Number of Blades (Z)	4
Hub-Diameter Ratio	0.300
Model Propeller Diameter	250.0 mm
Pitch-Diameter Ratio for $r/R=0.7$	1.239
Expanded Area Ratio,	0.5800
Propeller Rotational Direction	Right-Handed
Material of Model Propeller	Aluminum
Water Temperature	14.6°
Water Density	1002 kg/m ³

The propeller was designed and modeled based on a full-scale geometry. A right-handed Cartesian coordinate system was used in the propeller's hydrodynamic analysis. Thus, the x-axis indicated the axis passing through the centerline, the y-axis pointed out the upward direction of the propeller, and the z-axis direction followed the right-hand rule. The designed propeller and its coordinates are shown in Fig. 3.

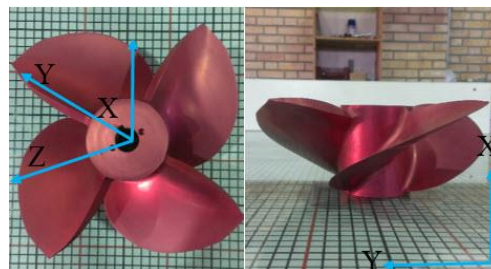


Fig. 3. Designed propeller and its coordinates.

3.2 Laboratory Specifications and Test Scenario

The propeller was subjected to open water tests in the towing tank of the National Iranian Marine Laboratory (NIMALA). Table 2 lists the specifications of the towing tank.

Table 2 The main particulars of the NIMALA towing tank

Length	400 m
Width	6 m
Depth	4 m
Maximum carriage speed	19 m/s

A reference calibration procedure was designed to ensure the reliability of the measurement process in the towing tank. In this regard, three aspects of the measurement, including tools, processes, and

uncertainty, were considered simultaneously. All sensors were carefully calibrated, and their data were meticulously acquired by an expert operator. Table 3 provides the technical characteristics of the measurement instruments.

Figure 4 demonstrates a view of the propeller position on the shaft in both stationary and rotational states. The installation and measurement method of the instruments were done based on the *ITTC (2008)* procedure.



Fig. 4. Propeller in the (a) stationary and (b) reactionary states.

SPPs usually operate for the planning phase in high-speed crafts at immersion ratios of less than 0.5. A boat's propeller is completely submerged until the planning phase, and a large torque is applied to its engine. The artificial aeration process can be employed for torque reduction when the propeller is completely submerged. To this end, the value of the propeller torque in a fully submerged state must be determined, and then the amount of mass flow in the artificial ventilation should be calculated. Accordingly, the fully submerged state was also examined in this article. Three immersion ratios were studied to investigate the different operating states of the SPP, which start from a submerged state and end up in a semi-submerged state. As shown in Fig. 5, an experimental test was performed at three immersion ratios of 0.4, 0.75, and 2 and a constant rotational speed of 9 RPS with 0.1 steps alternating advance coefficient from 0.2 to 1.2 by changing the advance velocity.

3.3 Experimental Results

Figure 6 depicts the hydrodynamic performance of the SPP at different immersion ratios. As can be seen, the critical advance coefficient in the thrust coefficient diagram decreases from 0.8 to 0.7 with the rise in the immersion ratio from 0.4 to 0.75.

Given the shortened length of the ventilation zone at greater immersion ratios and more relative contact of the key blade with water, the values of thrust and torque coefficients increased. On the other hand, with the rise in the immersion ratio, the growth rates of the thrust and torque coefficients of the key blade Moreover, for the advance coefficients of 0.8 and higher, the efficiency at the immersion ratio of 0.4 was higher than that at the immersion ratio of 0.75. Meanwhile, for the advance coefficients of lower than the mentioned value, the efficiency at the immersion ratio of 0.75 was higher.

It is worth mentioning that a higher thrust is available by increasing the immersion, but the torque needs to

be controlled. Also, for the torque generated more than the maximum allowed for the engine, the appropriate state can be achieved by reducing the immersion ratio. Therefore, it can be said that the

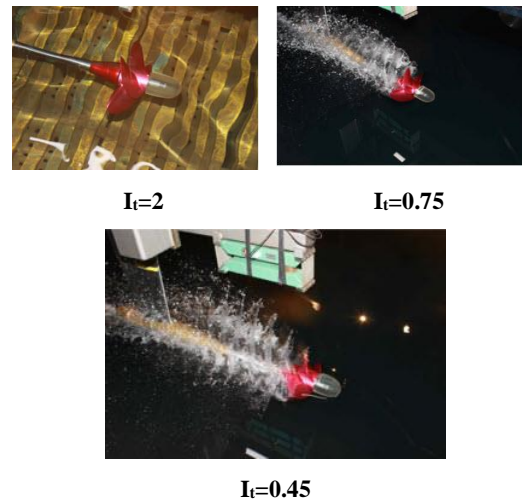


Fig. 5. Open water tests of the SPP at different immersion ratios.

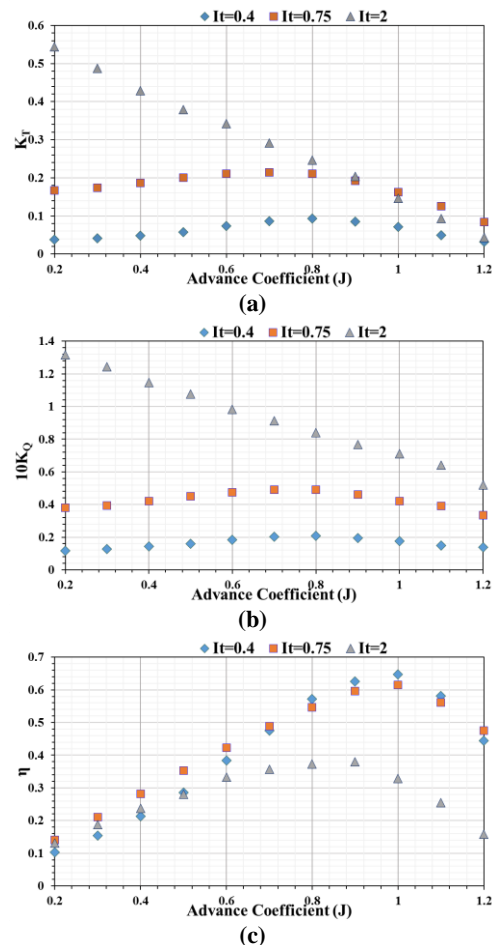


Fig. 6. (a) Thrust coefficients, (b) Torque coefficients, and (c) Efficiency coefficients at different immersion ratios.

best way to benefit from a high thrust at high immersion ratios and higher efficiency at lower immersion ratios is to use adjustable immersion drive systems. Consequently, these propellers with different capacities could be used in various conditions. In partially and fully ventilated areas were not the same. Therefore, the changes in the propeller efficiency were different.

Under the full submergence condition (immersion ratio of 2), the SPP acted like conventional propellers in hydrodynamic performance, and its efficiency was significantly lower than those at immersion ratios of 0.4 and 0.75.

4. NUMERICAL MODELING

4.1 Governing Equations

The homogeneous Eulerian multiphase model was used since the current study does not deal with substantial splashing around the blades. The two phases were considered continuous phases in a separated subsystem. In the homogeneous multiphase flow model, all fluids share the same velocity, temperature, and turbulence fields, but in the inhomogeneous model, each fluid's velocity, temperature, and turbulence fields are treated independently. The homogeneous Eulerian multiphase model is commonly applied to free surface flow with a distinct resolvable interface between air and water. The volume fraction of each phase indicates how much of the flow domain it occupies. The volume of a phase r could be calculated as follows (Ferziger et al. 2002):

$$V_r = \int_V \alpha_r dv, r = 1, 2 \tag{10}$$

where $\alpha_r (V_r/V)$ is the volume fraction of phase r . The volume fractions of each Eulerian phase must satisfy the following requirement and equal one.

$$\sum_{r=1}^2 \alpha_r = 1 \tag{11}$$

The governing equations in the two-phase flow field are conservation of mass and momentum equations, as represented below:

$$\frac{\partial}{\partial t} (\alpha_r \rho_r) + \nabla \cdot (\alpha_r \rho_r V) = 0 \quad r = 1, 2 \tag{12}$$

$$\frac{\partial}{\partial t} \rho V + \nabla \cdot (\rho V \times V) = \tag{13}$$

$$\nabla \cdot (-P + \mu((\nabla V) + (\nabla V)^T))$$

where ρ, μ, V , and P are the fluid's density, viscosity, velocity, and pressure, respectively. The simplified Navier–Stokes equations for the momentum in the turbulence regime and the effective incompressible fluid can be written as Eq. 14 (Ferziger et al. 2002):

$$\rho \left(\frac{\partial \bar{u}_i}{\partial t} + \bar{u}_j \frac{\partial \bar{u}_i}{\partial x_j} \right) = -\frac{\partial \bar{P}}{\partial x_i} + \frac{\partial}{\partial x_j} \left(\mu \frac{\partial \bar{u}_i}{\partial x_j} - \rho \overline{u'_i u'_j} \right) + \rho g_i \tag{14}$$

in which u_i and u_j are the velocity components in directions i and j , respectively. The SST model is a hybrid of the $k-\omega$ and $k-\epsilon$ models, employing an adequate convergence rate of the $k-\epsilon$ model in high Reynolds zones and the precision of the $k-\omega$ model near the wall. Furthermore, the $k-\omega$ turbulence model better estimates adverse pressure gradient boundary layer flows and flow separation. With the rise in the distance from the wall, the SST model converts $k-\omega$ to $k-\epsilon$ by utilizing a transform function. Thus, in this study, the $k-\omega$ SST model was applied to the model. According to $\rho \overline{u'_i u'_j}$ term, the $k-\omega$ SST turbulence model, used for CFD simulations, is described as Eq. (15) (Ferziger et al. 2002):

$$\begin{aligned} \frac{\partial \rho k}{\partial t} + \frac{\partial}{\partial x_j} \left(\rho u_j k - \left(\mu + \frac{\mu_t}{\sigma_k} \right) \frac{\partial \omega}{\partial x_j} \right) = \\ P_k - C_\mu \rho \omega k \frac{\partial \rho \omega}{\partial t} + \\ \frac{\partial}{\partial x_j} \left(\rho u_j \omega - \left(\mu + \frac{\mu_t}{\sigma_\omega} \right) \frac{\partial \omega}{\partial x_j} \right) = \\ \alpha \frac{\omega}{k} P_k - \beta \rho \omega^2 + 2(1 - F_1) \frac{\rho}{\sigma_\omega \omega} \frac{\partial k}{\partial x_j} \frac{\partial \omega}{\partial x_j} \end{aligned} \tag{15}$$

4.1.1 Free surface modeling

A free surface was created using the volume of the fluid model. Since the fluid had two important phases, instead of calculating each phase separately, the governing equations of the flow (i.e., the momentum and continuity equations) were solved concurrently for an effective fluid by changing the physical parameters. The physical parameters of fluid at each point in the solution domain could be defined using Eq. (16) (Hirt and Nichols 1981):

$$\begin{aligned} \rho_{\text{eff}} &= \alpha \rho_1 + (1 - \alpha) \rho_2 \\ v_{\text{eff}} &= \alpha v_1 + (1 - \alpha) v_{2i} \end{aligned} \tag{16}$$

Table 3 Characteristics of the measurement instruments

Sensor	Unit	Measurement accuracy	Measurement tools	Measurement calibration instrument	Sampling Rate
Velocity	m/s	0.02%	Rotary encoder	Velocity meter	100 Hz
Thrust	N	0.02%	Rotary load cell	Standard weight	1000 Hz
Torque	N.m	0.02%	Rotary torque meter	Standard weight	1000 Hz

in which $0 < \alpha < 1$ indicates that the cell is located at the free surface. The volume fraction transport equation was obtained using the continuity equation and can be written as follow due to the incompressibility of the flow:

$$\frac{\partial \alpha}{\partial t} + \nabla \cdot (\alpha \mathbf{u}) = 0 \quad (17)$$

4.2 Computational Domain and grid Generation

In order to calculate the open water characteristics, moving reference frames or sliding mesh methods are used. The sliding mesh method has high accuracy due to the simulation of non-continuous and rotational flow around the semi-submersible propeller, so it was used in this study. This method divides the flow field into rotating and stationary regions for the propeller model with a scale of 1:1. The rotating region was considered a cylinder with a diameter of $1.1D$, and the static region was considered a rectangular cube due to its resemblance to the natural test environment of the SPPs in the towing tank. In simulating a semi-submerged propeller, it is better to consider the most significant possible computational range of domain. However, it should be noted that a larger domain increases the number of grids and thus increase the computing computation time.

On the other hand, the bigger size of the domain affects the convergence of the solution and increases the accuracy of the results. Therefore, the best way is to find an optimum relationship between the solution and domain dimensions. Finally, after several simulations and initial investigations to solve a semi-submerged propeller, the domain with the following dimensions (Fig. 9) was found to be suitable. The propeller was adjusted at a distance of $4D$ behind the inlet and a distance of $12D$ in front of the outlet. The width and height of the domain were $8D$.

The mesh generation was applied in STAR-CCM+ commercial software. A hexagonal structured (trimmed) mesh was used for both rotating and stationary regions. A prismatic mesh was also produced on the boundary layer of propeller blades, hubs, and shafts to capture the actual flow around the walls. In addition, in order to reduce the computation time, the production of fine mesh in all areas of the flow field was avoided, and the finer mesh was applied only in the areas around the propeller, especially at the leading edge and the tip of the propeller blades, along with the area around the free surface of the water. Furthermore, since the $k-\omega$ SST turbulence model was used in grid generation, the non-dimensional normal distance y^+ of the first cell layer adjacent to the wall was kept well below 1.59 to resolve the near-wall boundary layer. According to Fig. 7, the average value of Y^+ is was below 1. Finally, in the present study, about 2.6M meshes were generated. The mesh generation around the SPP and the computational domain are shown in Fig. 8. As can be seen, the grid was fine near the surface of the water and the propeller, so the separation of the current as with the rotation of the propeller can be observed with the help of this simulation. Furthermore, the temporal discretization of the study was done such that in a time

step, the propeller rotated only through one degree, resulting in various time steps at different advance ratios. In addition, according to repeated simulations, in order to achieve convergence, the propeller had to rotate at least five complete revolutions.

4.3 Boundary Conditions

Boundary conditions of the simulation were selected regarding its physics. Accordingly, velocity inlet condition was used on the inlet; pressure outlet condition was applied to the outlet; symmetry plane condition was used on the left and right sides; and no-slip wall condition was applied to the top and bottom walls, propeller, hub, and shaft. Fig. 9 illustrates the computational domain and boundary conditions for the open water simulation of the SPP.

The velocity inlet condition with dimensionless turbulence intensity of 0.01 and a turbulent viscosity ratio of 10 was defined on the inlet boundary. The pressure outlet condition with boundary normal direction backflow specification was set on the outlet boundary. In order to connect the stationary and rotating regions, the domain used an internal interface with an in-place topology.

The volume fraction algorithm was utilized to profit the solution stability. Therefore, equations of volume fraction, velocity, and pressure were implicitly coupled by this algorithm.

4.4 Grid Independence Study

In order to study the grid independence and mesh quality, four grid configurations were generated using a base size refinement. The variation of open-water characteristics with the grid size was investigated. Table 4 lists the characteristics of the grids used to study the sensitivity of the results to the mesh. Moreover, Table 5 provides the results obtained for the independence of the mesh studied in this research for $I_t = 0.75$ and $J = 0.9$. As shown in Fig. 10, there was a big ascent of 1.67% in thrust coefficient when the number of cells grew from 0.695 to 1.761 million. Then, a rise of about 1.09% occurred in K_T from grid 2 (1.761 million) to grid 3 (2.593 million). Meanwhile, a minor growth of 0.54% was observed from grid 3 to grid 4 (4.218 million). Given the negligible growth in thrust coefficient results from grid 3 to grid 4 and the significant reduction of computational time, grid 3 was used for other simulations.

4.5 Sensitivity Study and Verification

The Grid Convergence Index (GCI) method was employed to validate the capability of the proposed CFD model and the present computer code (STAR CCM+) in solving the system of equations when fine grid resolution was applied. This approach is known as an acceptable and suggested way of evaluating the discretization error in CFD simulations (Celik *et al.* 2008).

Grid refinement factors r_{23} and r_{34} were computed as $r_{23}=h_2/h_3=1.2$ and $r_{34}=h_3/h_4=1.25$ for three sets of grids (grid 2, grid 3, and grid 4), where h_i is the size of the i^{th} grid. The method's apparent order, p_a , was computed as follows:

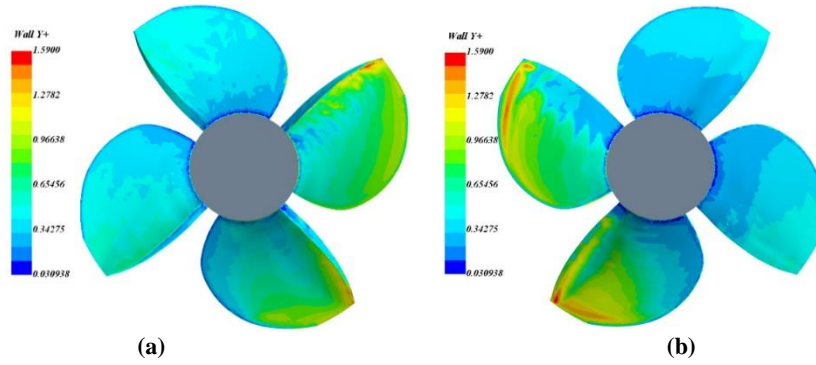


Fig. 7. Y^+ distribution on the (a) pressure side and (b) suction side.

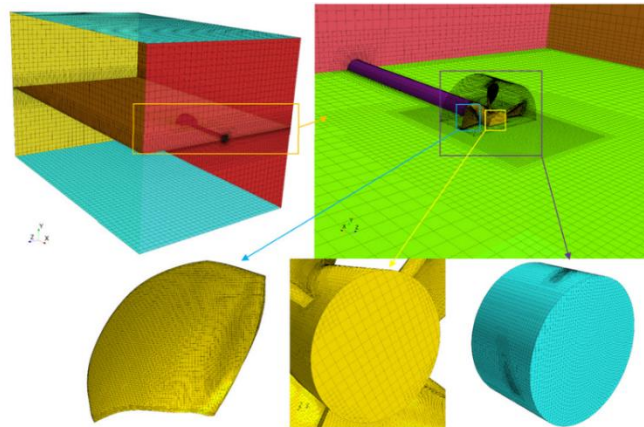


Fig. 8. A schematic of mesh generation.

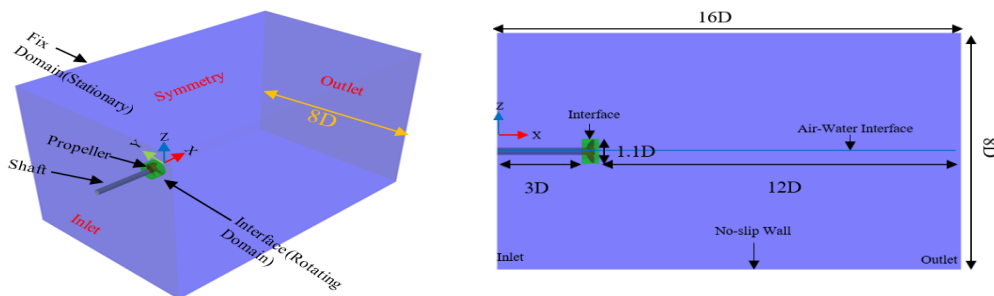


Fig. 9. Stationary and rotating computational domains and boundary conditions.

Table 4 Grid specifications for studying the mesh independence

	Grid 1	Grid 2	Grid 3	Grid 4
Cells in total	0.66e+6	1.77e+6	2.54e+6	4.12e+6
Cells in rotating domain	0.51e+6	1.16e+6	1.55e+6	2.26e+6
Base size	21 mm	12 mm	10 mm	8 mm
Prismatic layers number	12	12	12	12
Prism layer thickness	1.5 mm	1.5 mm	1.5 mm	1.5 mm

Table 5 Grid data for the grid independence study at $I_t=0.75$ and $J=0.9$

Mesh Configuration	Grid 1			Grid 2			Grid 3			Grid 4		
	K_T	$10K_Q$	η									
CFD results	0.179	0.509	0.504	0.182	0.503	0.518	0.186	0.471	0.566	0.187	0.47	0.570
EFD results	0.192	0.461	0.597	0.192	0.461	0.597	0.192	0.461	0.597	0.192	0.461	0.597
Error (%)	-6.77	10.41	-15.58	-5.21	9.11	-13.14	-3.13	2.17	-5.2	-2.6	1.95	-4.48

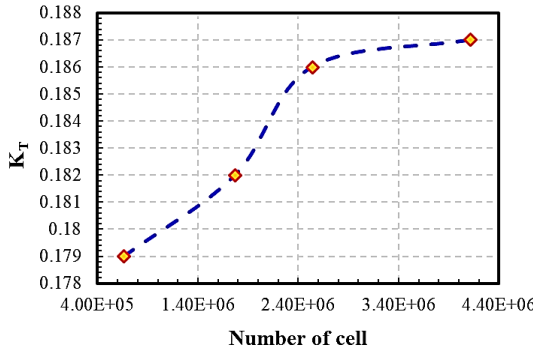


Fig. 10. The grid independence study at $I_t=0.5$ and $J=0.9$.

$$p_a = \frac{1}{\ln(r_{34})} \left| \ln \left| \frac{\varepsilon_{23}}{\varepsilon_{34}} \right| + q_{(p_a)} \right| \quad (18)$$

$$q_{(p_a)} = \ln \left(\frac{r_{34}^{p_a} - s}{r_{23}^{p_a} - s} \right) \quad (19)$$

$$s = 1 \cdot \text{sign}(\varepsilon_{23} / \varepsilon_{34}) \quad (20)$$

where $\varepsilon_{34} = \phi_3 - \phi_4$, $\varepsilon_{45} = \phi_4 - \phi_5$, and ϕ_k is the key variable on the k^{th} grid. The extrapolated values were produced using the following formula:

$$\phi_{\text{ext}}^{34} = \left(\frac{r_{34}^{p_a} \phi_4 - \phi_3}{r_{34}^{p_a} - 1} \right) \quad (21)$$

The equations below were used to compute the approximate and extrapolated relative errors.

$$e_a^{34} = \left| \frac{\phi_4 - \phi_3}{\phi_4} \right| \quad (22)$$

$$e_{\text{ext}}^{34} = \left| \frac{\phi_{\text{ext}} - \phi_4}{\phi_{\text{ext}}} \right| \quad (23)$$

The fine-grid convergence index was calculated by:

$$GCI_{\text{fine}}^{34} = 1.25 e_a^{34} / (r_{34}^{p_a} - 1) \quad (24)$$

Table 6 shows the discretization error calculations for the three selected grids. As can be observed, the estimated values of K_T and K_Q had numerical errors of 0.113% and 0.0038%, respectively.

5. NUMERICAL RESULTS

The average values of K_T , K_Q , and η were measured and calculated in the experimental test and the numerical simulation, respectively. The diagram of hydrodynamic coefficients at different advance velocities and immersion depths in the experimental test and the numerical simulation are shown in Fig. 11. According to the figure, a great agreement existed between the results of the experimental test and the numerical solution.

Table 6: The discretization error of K_T and K_Q values

Parameters	K_T	K_Q
r_{23}	1.2	1.2
r_{34}	1.25	1.25
ϕ_2	0.182	0.0503
ϕ_3	0.186	0.0471
ϕ_4	0.187	0.047
p_a	8.046	19.102
ϕ_{ext}^{34}	0.187	0.047
e_a^{34}	0.005	0.002
e_{ext}^{34}	0.001	0.0004
GCI_{fine}^{34}	0.133 %	0.0038 %

Figure 12 illustrates the error of the numerical method compared to the experimental results. As can be seen, the greatest differences between the numerical and experimental results in the thrust coefficient, torque coefficient, and efficiency were about 6.33%, 7.1%, and 7.42%, respectively. According to the figure, the numerical solution well agreed with the experimental results.

It is essential to consider the forces and torques applied to the blades at different stages from the moment of entry till coming out of the water, which depend on the immersion ratio. Therefore, it is important to consider the different angular positions of one blade, which is called the key blade, as shown in Fig. 13.

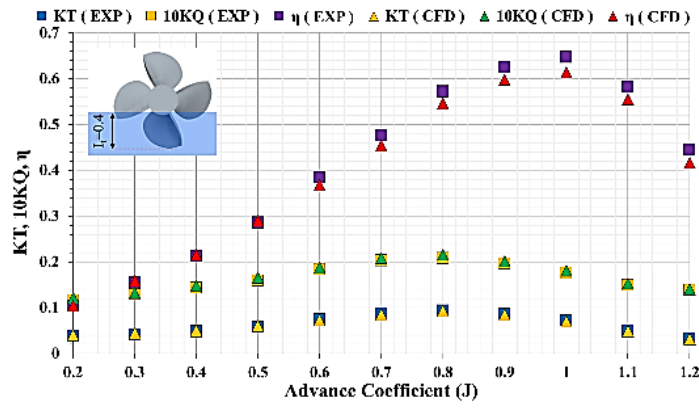
According to the coordinate system shown in Fig. 3, the six components of force and moment coefficients on the key blade can be defined as follows respectively:

$$K_{FX, FY, FZ} = \frac{F_{X,Y,Z}}{\rho n^2 D^4} \quad (25)$$

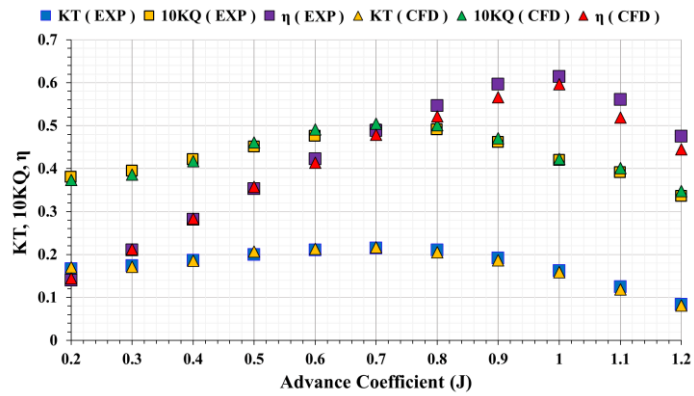
$$K_{MX, MY, MZ} = \frac{M_{X,Y,Z}}{\rho n^2 D^5} \quad (26)$$

Figures 14-16 depict the average loads measured on the key blade in the hub fixed coordinate system for different advance ratios at different immersion depths.

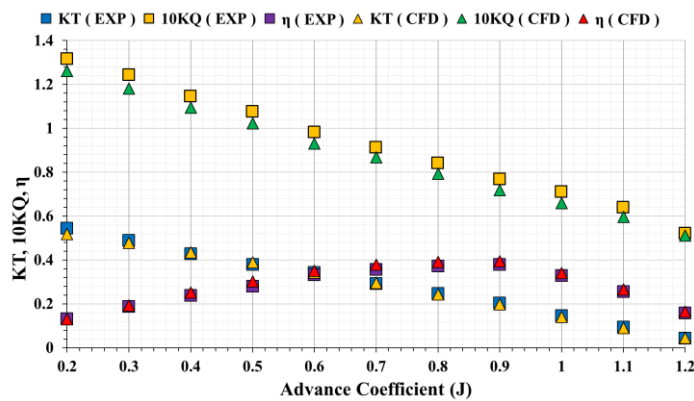
As can be seen, at a particular advance coefficient in the partially submerged state of the propeller, K_{FX} and K_{MZ} are the maximum force and moment coefficients for the key blade. On the other side, the F_y force component plays an important role in generating K_{MX} torque between its maxima and minima. Afterward, the value of K_{MX} lowers to zero with a high gradient.



(a)

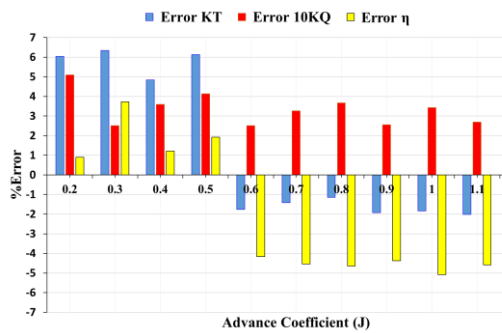


(b)

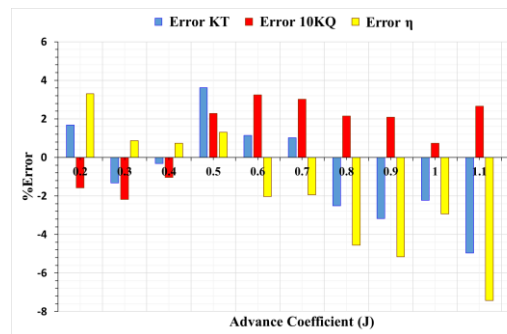


(c)

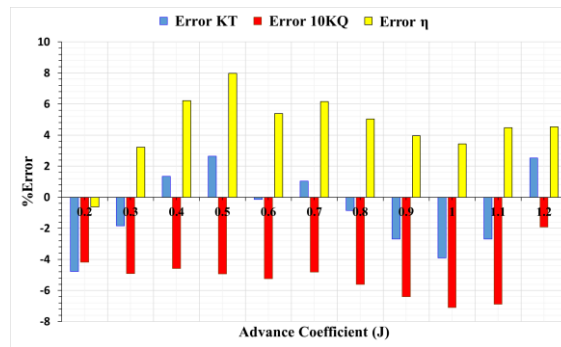
Fig. 11. Hydrodynamic coefficients at the immersion ratios of 0.4 (a), 0.75 (b), and 2 (c).



(a)



(b)



(c)

Fig. 12. Error rate between the numerical solution and experimental results at immersion ratios of 0.4 (a), 0.75 (b), and 2 (c).

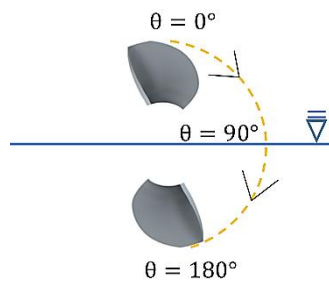


Fig. 13. Angular position of the key blade.

The thrust fluctuated at different depths, but the tendency to fluctuate varied with the immersion depth. The fluctuations were larger at shallower immersion depths.

According to Figs. 14 and 15, once the blade hit the water surface, strong jets were created around the leading edge of the blade, resulting in a larger wet surface on the face side of the blade, as well as heavy impact loads. This phenomenon effectively participated in hydrodynamic loads during the blade entry phase.

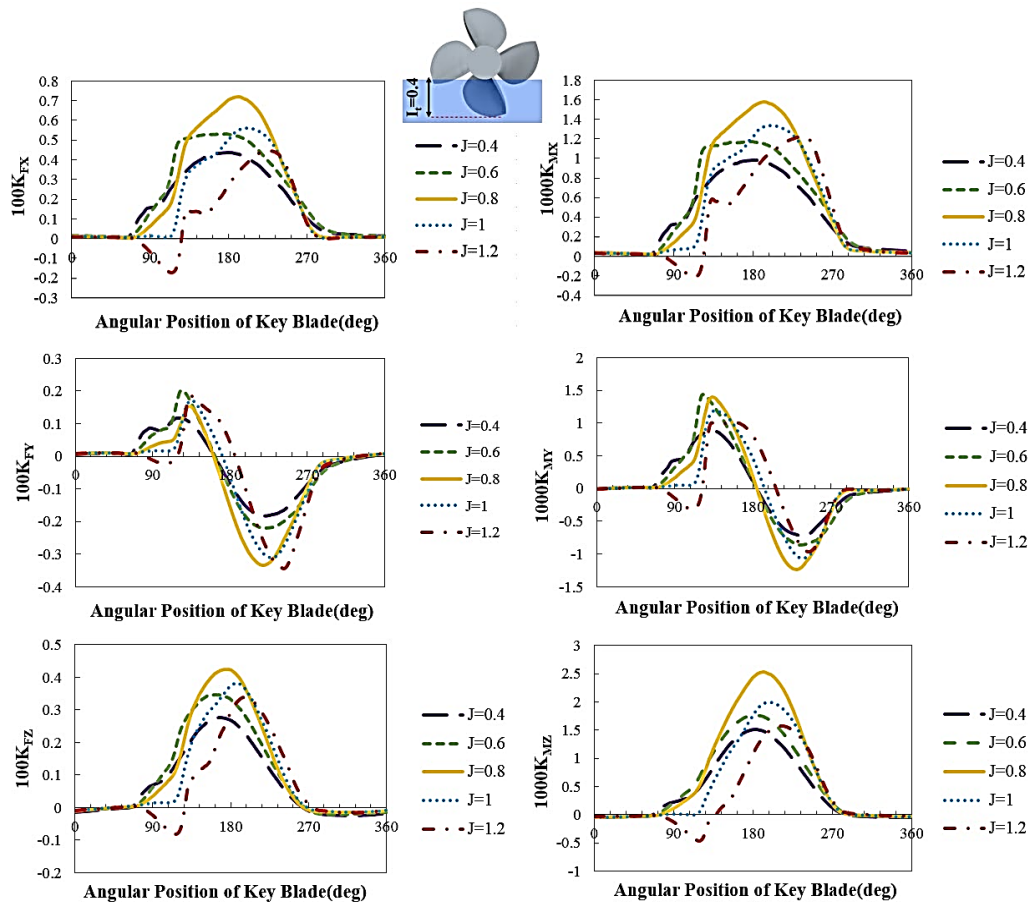


Fig. 14. Calculated rotational fluctuations of the six force/moment components versus the angular position of the key blade at $I_t=0.4$ and different advance ratios.

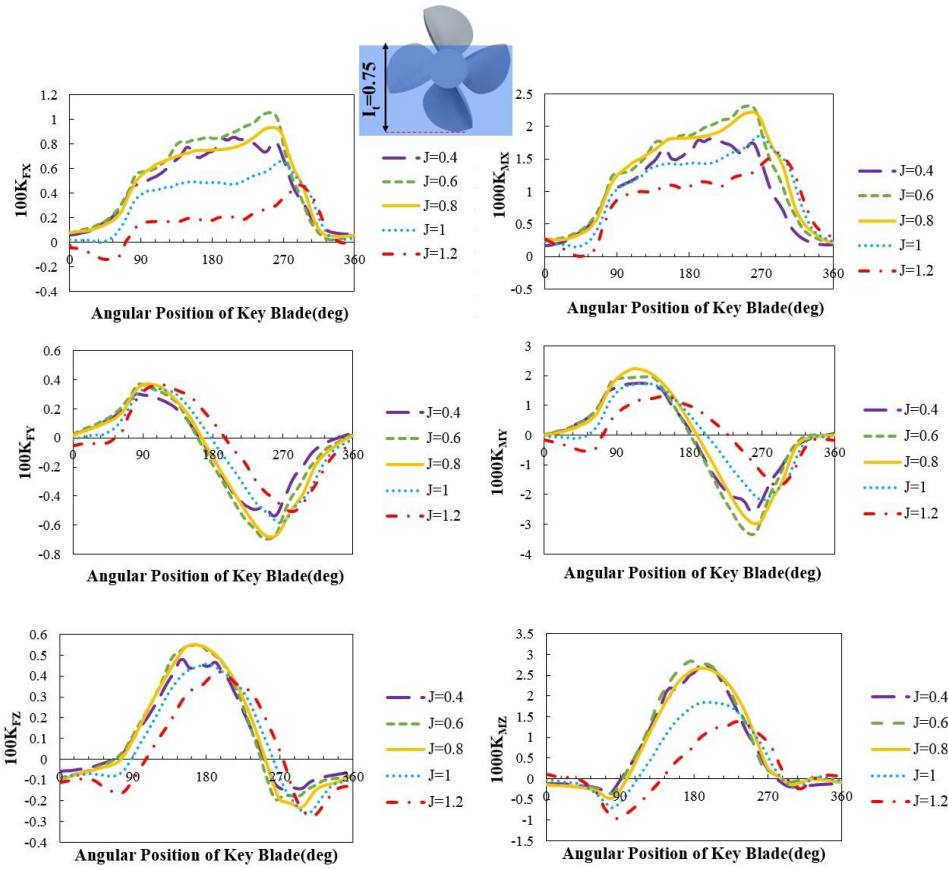


Fig. 15. Calculated rotational fluctuations of the six force/moment components versus the angular position of the key blade at $I_t=0.75$ and different advance ratios..

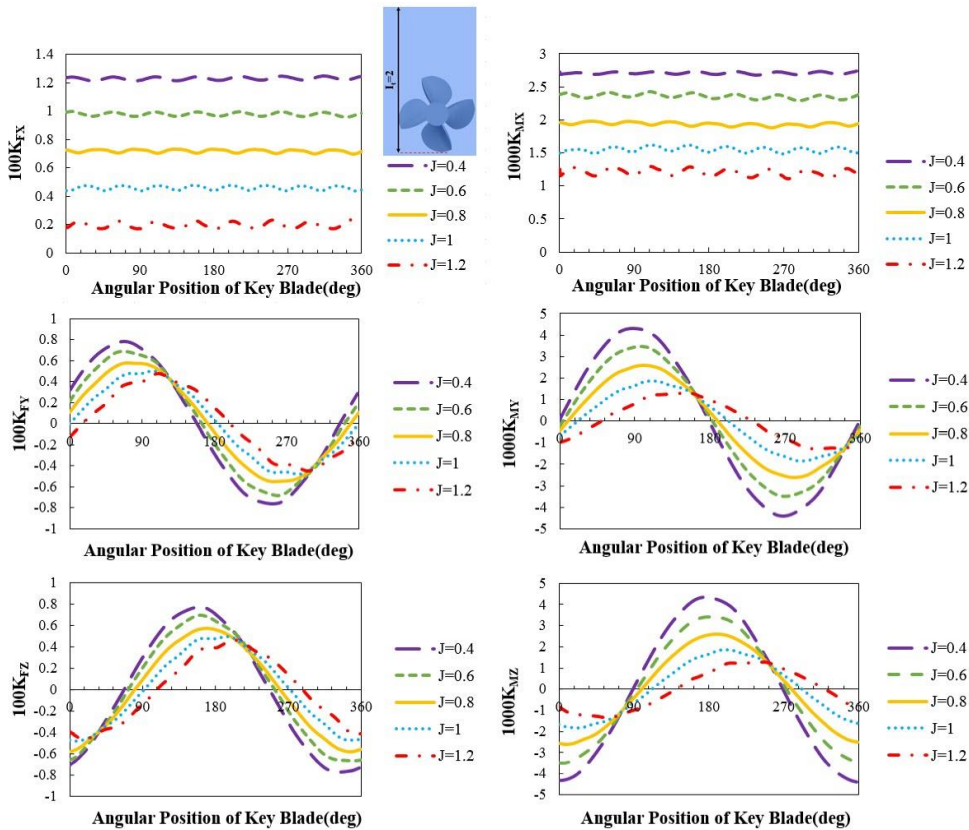


Fig. 16. Calculated rotational fluctuations of the six force/moment components versus the angular position of the key blade at $I_t=2$ and different advance ratios.

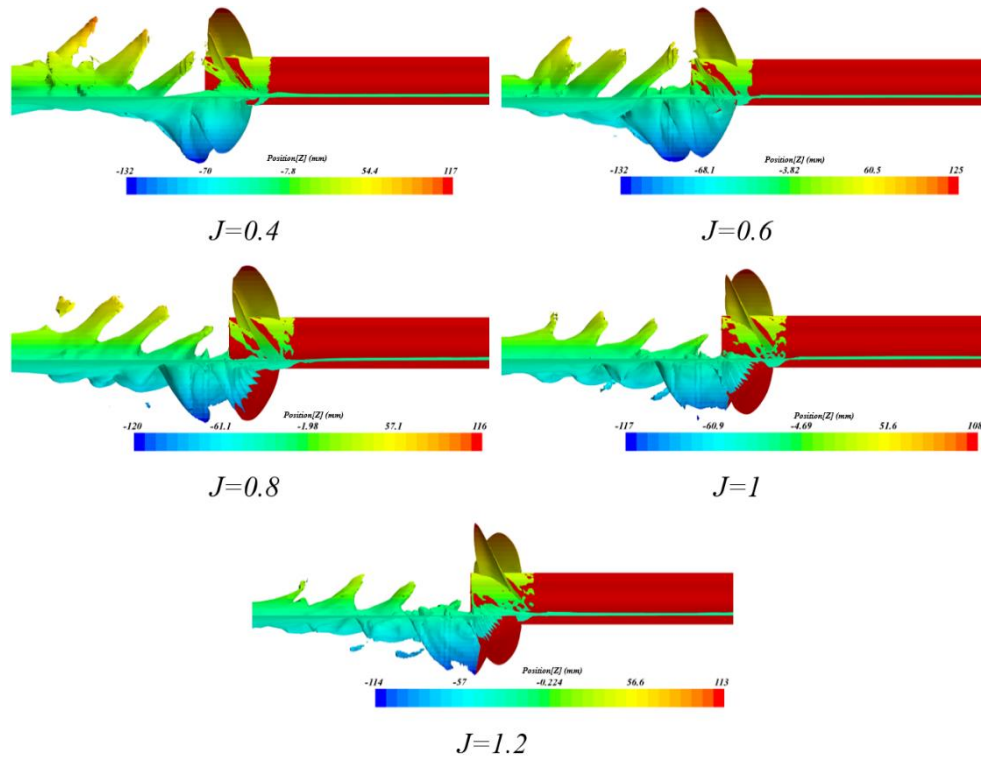


Fig. 17. Predicted wave pattern on the free surface for immersion ratio of 0.4 and different advance coefficients.

Therefore, the volume fraction of water on both sides of the blade, i.e., the pressure side and the suction side, increased with the advance ratio. The volume of water leaving the free surface also increased, resulting in a drag and thus energy loss and lower blade efficiency. In other words, by increasing the advance coefficient to a value higher than the critical value for the propeller, in the initial interval of entering the key blade into the water, the six components of the force and moment were reduced, and the thrust and drag balance changed such that for advance coefficients of 1.2 and higher, the drag is generated at first and then the thrust was created until the key blade came out of the water. It is noteworthy that the key blade drag was negligible compared to its maximum generated thrust.

A comparison between Figs. 14-16 reveals that for most advance coefficients, the amplitude of the six force/moment components of the key blade increased with the immersion depth.

Figures 17 shows the predicted wave pattern for immersion ratio of 0.4 and different advance coefficients. Since the homogeneous Eulerian multiphase model was used in this study, air and water were treated as continuous phases in a separated system. As a result, no substantial splashing could be produced around the blades. To cope with splashing around the propeller, an inhomogeneous multiphase flow model, as well as mixture or particle methods, which are substantially more time-intensive and complex, had to be utilized. However, the method used in this investigation could accurately forecast the flow pattern around the propeller. Fig. 17 shows, the amount of water spray

decreased at higher advance coefficients.

Since one of the crucial issues in this type of propeller is the amount of ventilation on the blades, it was also investigated, and it was found that the trailing edge of SPPs is more ventilated than their leading edge. Fig. 18 demonstrates the volume fraction of air on the key blade for different advance coefficients at an angular position of 180°. Besides, Fig. 19 shows the ventilation pattern from the moment the key blade entered the water at the immersion ratio of 0.4 and different advance coefficients. As understood from the figures, when the advance coefficient decreased, the ventilation zone grew up. That is, at advance coefficients above the critical value in immersion depth of 0.4, which was equal to 0.8, no air entered the blade's leading edge. When the advance coefficient was lower than the critical value, ventilation started from the blade's trailing edge, and with a reduction of the advance coefficient, the amount of aeration on the suction side of the propeller increased. It was also found that the volume fraction of air on the pressure side of the key blade did not change significantly with increasing the advance coefficient, while the volume fraction of the air on the suction side decreased remarkably.

Figures 20 depicts the volume fraction of water on the key blade on the pressure and suction sides at different immersion ratios with an advance coefficient of 0.6 and an angular position of 180°. As can be deduced from the figure, the ventilation decreased at higher immersion ratios. More precisely, ventilation occurred at $I_t=0.4$, while at $I_t=0.75$, lower ventilation levels were observed on both

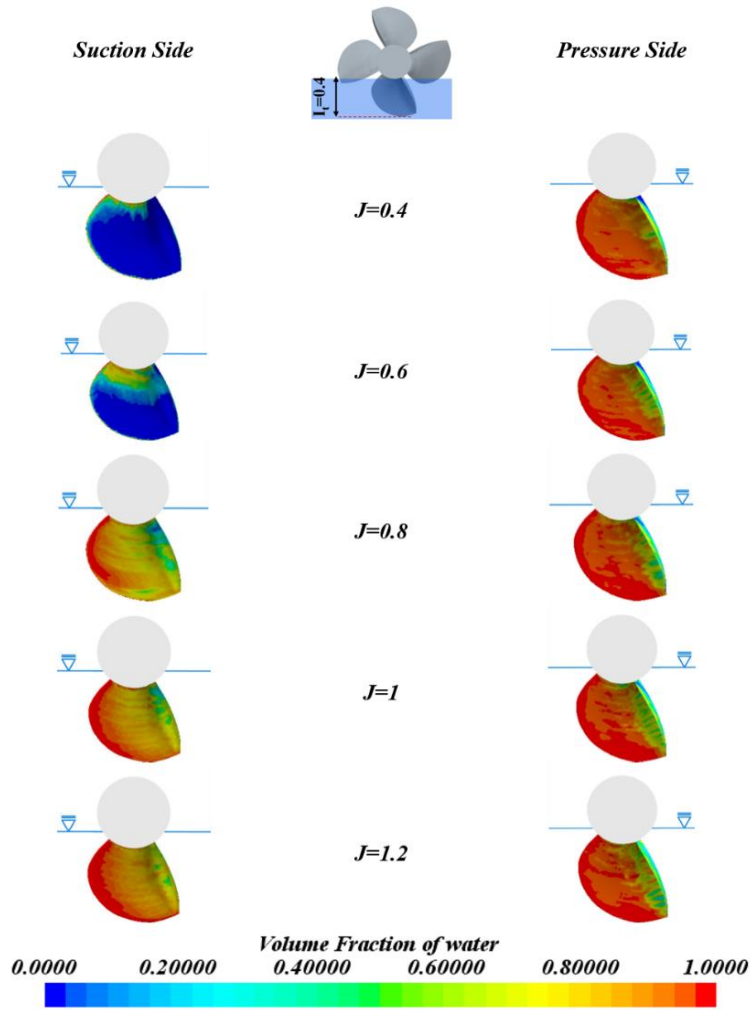


Fig. 18. VOF of water at the back and face of the key blade for $I_t=0.4$ and different values of J .

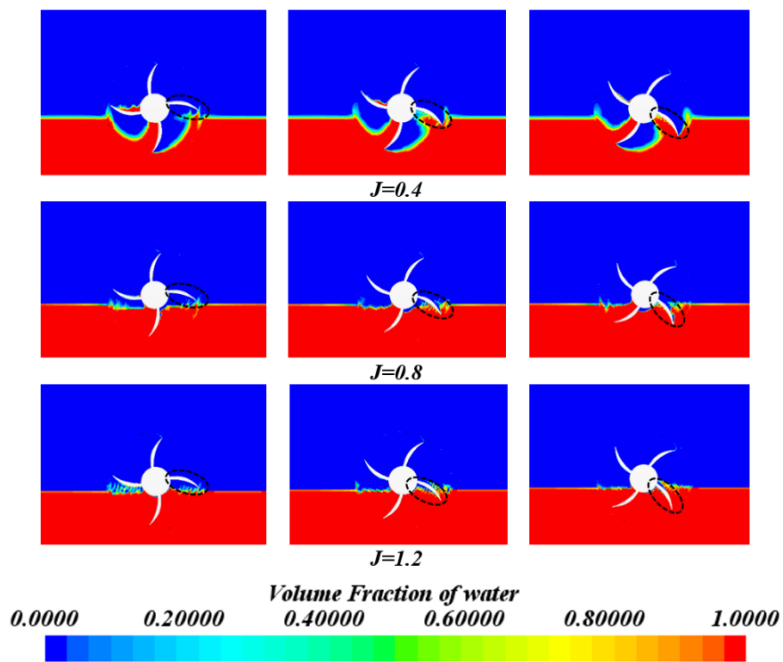


Fig. 19. VOF pattern on the cross-section of the SPP for $I_t=0.4$ and different advance ratios.

pressure and suction sides, and at $I_t = 2$, the propeller was completely submerged without any ventilation.

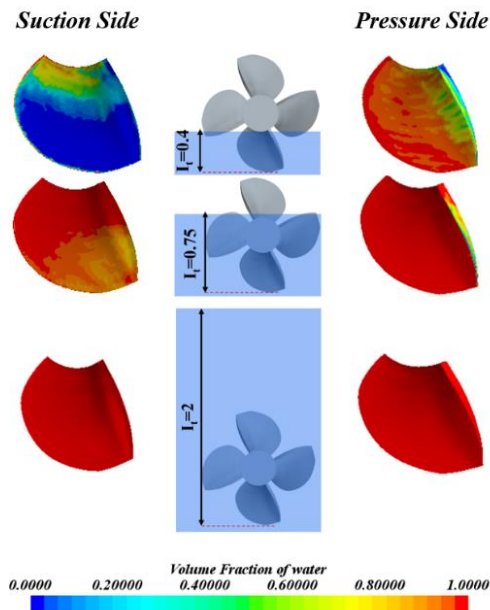


Fig. 20. VOF of water at the back and face of the key blade for $J=0.6$ and different values of I_t .

In this study, the pressure coefficient, calculated as $C_p = 2(P - P_{atm}) / (\rho(0.7\pi nD)^2)$, was used for pressure distribution investigations on the propeller key blade.

The graphs of the pressure coefficient for various advance coefficients in Fig. 21 show that the pressure distribution on the leading edge was higher than that on the trailing edge. The effects of impact on the leading edge were responsible for this substantial discrepancy. Investigating the blade's suction surface side revealed that some spots in contact with water had a negative pressure, resulting in a sharp drop in the pressure coefficient near the leading edge. The pressure increased with the travel from the leading edge to the trailing edge and approached atmospheric pressure at the beginning point of the ventilation. Hence, the pressure coefficient at the trailing edge and ventilated portions became zero. As a result, the pressure coefficient near the leading edge tended to be constant in low advance coefficients, and the value near-zero thus ventilation occur. The region with the zero pressure coefficient tended to reduce x/C values with the rise in the advance coefficient.

The pressure distribution of the fluid on the key blade at different submergences in Fig. 22 shows that the pressure on the propeller's key blade increased with the immersion ratio. The pressure distribution processes on the key blade in fully and partially submerged propeller situations had a similar trend. Unlike in the fully submerged mode, in the partially submerged mode, the pressure coefficient approached zero in some areas close to the leading and trailing edges. This position indicated the amount of aeration on the key blade.

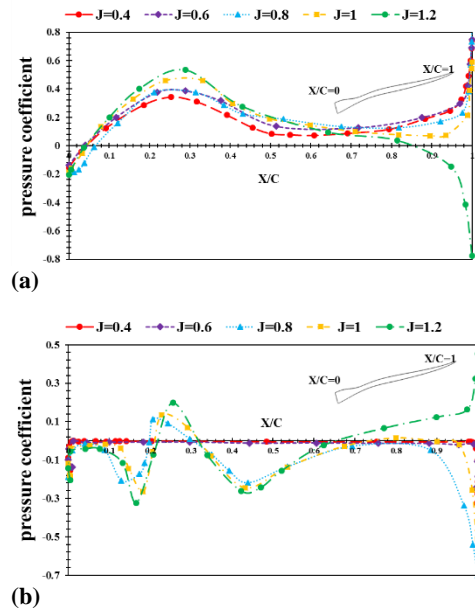


Fig. 21. Pressure coefficient distribution on the key blade at $r/R=0.7$ for various advance coefficients in immersion ratio of 0.4: (a) Pressure side, (b) Suction side.

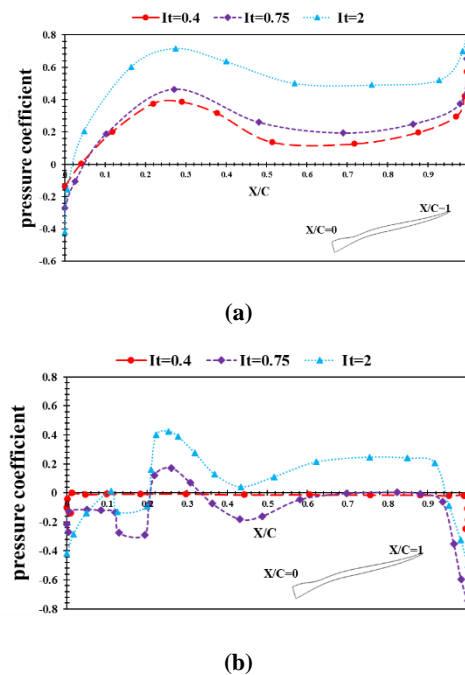


Fig. 22. Pressure coefficient distribution on the key blade at $r/R=0.7$ for the advance coefficient of 0.6 and various immersion ratios: (a) Pressure side (b) Suction side.

6. CONCLUSION

In this study, the hydrodynamic performance of a four-blade semi-submersible propeller with a pitch ratio of 1.239 and a diameter of 250 mm was investigated using computational fluid dynamics and an experimental test in a towing tank. The RANS was used along with the VOF method to simulate the

fluid around the SPP in the numerical method. In order for validation, the results were compared with the data measured in NIMALA. The conclusions of this research are as follows:

- The maximum error of the thrust and torque coefficients and efficiency obtained from the numerical method compared to the experimental data was approximately 6.33%, 7.1%, and 7.42%, respectively. Indeed, the experimental data confirmed the numerical method.
- According to the results, the thrust and torque coefficients of SPP increased with the rise in the immersion depth, but the efficiency acted differently. Furthermore, the critical advance coefficient reduced as the immersion ratio increased. At $I_t=2$, the hydrodynamic performance of the semi-submersible propeller was like that of the fully submersible propeller.
- At a particular advance coefficient in the partially submerged state, the maximum force and torque applied to the blades from the moment of water entry till the exit are K_{FX} and K_{MZ} . Moreover, the formation of K_{MX} torque was mainly affected by F_Y force.
- Due to the heavy impact loads, when the blade entered the water, it produced drag that caused six force and moment components reduction. It is necessary to mention that the total generated thrust of each blade was much higher than its drag.
- At a constant advance coefficient, studying three immersion ratios indicated that at a lower immersion ratio ($I_t=0.4$), the key blade pierced the surface more effectively at the entering phase. Therefore, the ventilation cavity length increased, and a larger cavity formed such that almost the entire suction surface of the blade was ventilated, and the cavity length reached the trailing edge of the key blade. With the rise in the immersion ratio in the surface piercing mode, ventilation on the suction side and at the trailing edge of the key blade decreased.
- The ventilation in pressure and suction surface sides at $I_t=0.4$ showed that almost the entire suction surface of the key blade area was in contact with air at the advance coefficients lower than the critical value ($J=0.8$). By increasing the advance coefficient to values higher than $J=0.8$, the length of the aeration at suction surface side of the key blade was significantly reduced due to the transfer to the partial ventilation zone.
- The ventilation pattern of the semi-submersible propeller decreased with the rise in the advance coefficient at a constant I_t . In detail, as the advance coefficient

increased, no changes were observed in air volume fraction on pressure side of the key blade, while on the suction side, the reduction was noticeable. In addition, as the I_t increased for a constant advance coefficient, the ventilation pattern was reduced so that it did not occur at $I_t=2$.

- The pressure coefficient revealed the impact's consequences on the leading edge. The pressure on the leading edge was greater than trailing edge. The pressure on the suction surface side of the blade rose from the leading edge to the trailing edge until approaching air pressure at the start point of the ventilation. The zone with zero pressure coefficient tended to lower x/C values as the advance coefficient grew.
- Study of pressure distribution on the key blade at different submergence depths indicated that the rise in the immersion ratios resulted in higher pressure coefficients on the pressure and suction sides of the propeller.

REFERENCES

- Alimirzazadeh, S., S. Z. Roshan and M. S. Seif (2016). Unsteady RANS simulation of a surface piercing propeller in oblique flow. *Applied Ocean Research* 56, 79-91.
- Brandt, H. (1973). Modellversuche mit Schiffspropellern an der Wasseroberflaeche. *Schiff und Hafen*, 5.
- Caponnetto, M. (2003, October). RANSE simulations of surface piercing propellers. In *Proceedings of The 6th Numerical Towing Tank Symposium*.
- Celik, I. B., U. Ghia, P. J. Roache and C. J. Freitas (2008). Procedure for estimation and reporting of uncertainty due to discretization in CFD applications. *Journal of fluids Engineering-Transactions of the ASME*, 130(7).
- Fernando, M., A. Scamardella, N. Bose, P. Liu and B. Veitch (2002). Performance of a family of surface piercing propellers. Royal Institution of Naval Architects. *Transactions. Part A. International Journal of Maritime Engineering*, 144(Part A1), 63-77.
- Ferziger, J. H., M. Perić and R. L. Street (2002). *Computational methods for fluid dynamics* (Vol. 3, pp. 196-200). Berlin: springer.
- Ghassemi, H., R. Shademani and A. Ardeshir (2009, January). Hydrodynamic characteristics of the surface-piercing propeller for the planing craft. In *International Conference on Offshore Mechanics and Arctic Engineering* (Vol. 43444, pp. 589-595).
- Ghose, J. P. (2004). *Basic ship propulsion*. Allied publishers.
- Hadler, J. B. (1968). Performance of partially

- submerged propellers. *7th ONR Symposium on Naval Hydrodynamics-Rome, (August 1968)*.
- Hecker, R. (1973). *Experimental performance of a partially submerged propeller in inclined flow* (No. Paper F).
- Himeï, K. (2013, May). Numerical analysis of unsteady open water characteristics of surface piercing propeller. In *Third International Symposium on Marine Propulsors smp* (Vol. 13, pp. 292-297).
- Himeï, K. and H. Yamaguchi (2015, September). Numerical Study on Performance of Surface Piercing Propeller using RANS Approach. In *SNAME 13th International Conference on Fast Sea Transportation*. OnePetro.
- Hirt, C. W. and B. D. Nichols (1981). Volume of fluid (VOF) method for the dynamics of free boundaries. *Journal of computational physics* 39(1), 201-225.
- ITTC-Recommended Procedures and Guidelines* (2005), Model Manufacture, Propeller Models Propeller Model Accuracy.
- ITTC-Recommended Procedures and Guidelines* (2008), Testing and Extrapolation Methods Propulsion, Propulsor Open Water Test.
- Javanmard, E., E. Yari and J. A. Mehr (2020). Numerical investigation on the effect of shaft inclination angle on hydrodynamic characteristics of a surface-piercing propeller. *Applied Ocean Research* 98, 102108.
- Javanmard, E., E. Yari, J. A. Mehr and S. Mansoorzadeh (2019). Hydrodynamic characteristic curves and behavior of flow around a surface-piercing propeller using computational fluid dynamics based on FVM. *Ocean Engineering* 192, 106445.
- Kozłowska, A. M., K. Wöckner, S. Steen, T. Rung, K. Koushan, and S. Spence (2011). Numerical and experimental study of propeller ventilation." *Second International Symposium on Marine Propulsors, Hamburg, Germany*.
- Kruppa, C. (1972). Testing of partially submerged propellers. *13th ITTC-Berlin, (September 1972)*.
- Kruppa, C. F. (1992). Testing surface piercing propellers. *13th ITTC-Berlin* (September 1972).
- Misra, S. C., R. P. Gokarn, O. P. Sha, C. Suryanarayana and R. V. Suresh (2012). Development of a four-bladed surface piercing propeller series. *Naval Engineers Journal* 124(4), 105-138.
- Nouroozi, H. and H. Zeraatgar (2019). A reliable simulation for hydrodynamic performance prediction of surface-piercing propellers using URANS method. *Applied Ocean Research* 92, 101939.
- Oberembt, H. (1968). *Zur bestimmung der instationären flügelkräfte bei einem propeller mit aus dem wasser herausschlagenden flügeln*. Technical report, Inst. für Schiffbau der Universität Hamburg, Bericht Nr. 247.
- Olofsson, N. (1996). *Force and flow characteristics of a partially submerged propeller*. Chalmers University of Technology.
- Rad, R. G., R. Shafaghat and R. Yousefi (2019). Numerical investigation of the immersion ratio effects on ventilation phenomenon and also the performance of a surface piercing propeller. *Applied Ocean Research* 89, 251-260.
- Rains, D. A. (1981, May). Semi-submerged propellers for monohull displacement ships. In *Propeller'81 Symposium* (pp. 15-40).
- Rose, J. C. and C. F. Kruppa (1991). *Methodical series model test results*. FAST '91, Trondheim Norway 1991.
- Rose, J. C., C. F. Kruppa and K. Koushan (1993). Surface Piercing Propellers, Propeller/Hull Interaction, FAST'93.
- Savineau, C. and S. Kinnas (1995). A numerical formulation applicable to surface piercing hydrofoils and propellers. In *24th American Towing Tank Conference, Texas A&M University, College Station, TX*.
- Shiba, H. (1953). Air-drawing of marine propellers. *Report of transportation technical research institute* 9 (1953): 1-320.
- Wang, G. and D. Jia (1990). Hydrodynamic performance of partially submerged ventilated propeller. *shipbuild, china*2.
- Wang, G., D. Jia and Z. Sheng (1992). Study on propeller characteristics near water surface. In *Proc 2nd Symp on Propeller & Cavitation, Hangzhou, China, ppl61-168*.
- Wang, G., X. Zhu and Z. Sheng (1990). Hydrodynamic forces of a three dimensional fully ventilated foil entering water. *Journal of Hydrodynamics* 2, 186-195.
- Yang, D., Z. Ren, Z. Guo and Z. Gao (2018). Numerical analysis on the hydrodynamic performance of an artificially ventilated surface-piercing propeller. *Water* 10(11), 1499.
- Yari, E. and H. Ghassemi (2016a). Hydrodynamic analysis of the surface-piercing propeller in unsteady open water condition using boundary element method. *International Journal of Naval Architecture and Ocean Engineering* 8(1), 22-37.
- Yari, E. and H. Ghassemi (2016b). Numerical analysis of surface piercing propeller in unsteady conditions and cupped effect on ventilation pattern of blade cross-section. *Journal of Marine Science and Technology* 21(3), 501-516.
- Young, Y. L. and S. A. Kinnas (2003a). Analysis of

- supercavitating and surface-piercing propeller flows via BEM. *Computational Mechanics* 32(4), 269-280.
- Young, Y. L. and S. A. Kinnas (2003b). Numerical modeling of supercavitating propeller flows. *Journal of Ship Research* 47(01), 48-62.
- Young, Y. L. and S. A. Kinnas (2004). Performance prediction of surface-piercing propellers. *Journal of Ship Research* 48(4), 288-304.
- Young, Y. L. and B. R. Savander (2011). Numerical analysis of large-scale surface-piercing propellers. *Ocean engineering* 38(13), 1368-1381.